Global NEST Journal, Vol 25, No X, pp 1-13
Copyright© 2023 Global NEST
Printed in Greece. All rights reserved

Preparation of mesoporous TiO_2 nanomaterials doped with rare earth ions (La^{3+}, Sm^{3+}, Nd^{3+}, Gd^{3+}) and its application in the photodegradation of unsymmetrical dimethylhydrazine wastewater

Yizhi Zeng and Xianghong Ren*
Xi'an Research Inst. of Hi-Tech, Xi'an 710025, China
Received: 03/08/2023, Accepted: 15/08/2023, Available online: 07/09/2023
*to whom all correspondence should be addressed: e-mail: renxh701@163.com
https://doi.org/10.30955/gnj.005280

Graphical abstract

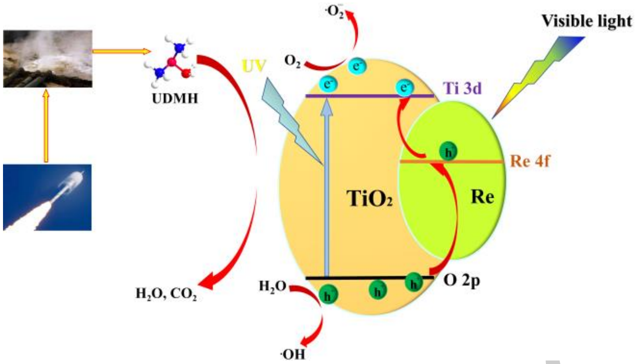

Abstract

Methyldimethylhydrazine and its by-products cause serious damage to human health. In this paper, Re^{3+}-doped mesoporous TiO_2 were synthesized for the photodegradation of UDMH. The structure, morphology and optical properties of photocatalyst were extensively characterized. The photocatalytic degradation was significantly enhanced, and 2%Nd-TiO_2 showed the most excellent photocatalytic degradation performance with 93.3% degradation rate of UDMH. NDMA and FDMH were gradually and completely degraded. O_2^- and·OH played an important role in the photocatalytic degradation of UDMH. The possible degradation pathways of UDMH analyzed by GC-MS. The work provided an effective method for the degradation of UDMH wastewater.

Keywords: mesoporous TiO_2, degradation, unsymmetrical dimethylhydrazine

1. Introduction

UDMH has been widely used as a high-energy liquid rocket fuel for missile weapons and aerospace applications because of its high specific impulse, low cost and easy storage. (Liu *et al.*, 2012) In the process of space launch, engine testing, fuel storage and transportation, a large amount of UDMH exhaust gas and waste liquid will be generated, which is prone to cancer and genetic mutation. (Carlsen *et al.*, 2009) The transformation products of UDMH such as nitrosodimethylamine (NDMA) and metahydrazone (FDMH) are highly carcinogenic [Sgroi *et al.*, 2018), Therefore, it is of great practical significance to study the degradation and mineralization methods of methyldimethylhydrazine. Traditional treatment methods of methyldimethylhydrazine mainly include physical treatment, chemical treatment and biological treatment. Traditional physical treatment methods such as activated carbon adsorption and ion exchange can remove UDMH from wastewater smoothly, but activated carbon and ion exchange resin cannot be regenerated and recycled, which is easy to cause secondary pollution. (FleMing *et al.*, 1996) Chemical treatment methods such as H_2O_2/O_3/UV degradation of UDMH in wastewater (Ismagilov *et al.*, 2002). Such methods are costly, energy intensive, and require MnO_2 and other substances to degrade the excess H_2O_2 in the experiment, and O_3 will corrode the experimental equipment. Biological treatment methods mainly use aquatic plant absorption method and microbial degradation treatment, the treatment cycle is long and slow, and it is difficult to deal with large-scale high concentration of UDMH wastewater, and the above traditional methods all have certain defects.

Photocatalysis is a sustainable oxidation technology that directly uses solar energy and is an effective solution for degrading pollutants in water bodies (Rueda-Marquez *et al.*, 2020). TiO_2 photocatalysts are green and economical, highly active and non-selective in the degradation of water pollutants (Rashid *et al.*, 2023) which can mineralize potential pollutants into non-polluting substances, and is a hot spot for photocatalyst research (Gopinath *et al.*, 2020; Rahman *et al.*, 2023; Malik *et al.*, n.d.), However, the currently prepared TiO_2 photocatalytic materials generally have a wide band gap (3.0~3.2eV) responding to UV light only, with only 4%-5% of the available solar energy, limited use in visible light (400 nm < λ < 700 nm), and high photogenerated electron and hole complexation rates with low catalytic efficiency (Byrne *et al.*, 2018).It is found that doping can extend the spectral response range and reduce the complexation rate of electron-hole pairs,

Zeng Y. and Ren X. (2023), Preparation of mesoporous TiO_2 nanomaterials doped with rare earth ions (La^{3+}, Sm^{3+}, Nd^{3+}, Gd^{3+}) and its application in the photodegradation of unsymmetrical dimethylhydrazine wastewater, *Global NEST Journal*, **25**(XX), 1-13.

thus improving the photocatalytic performance (Paradisi et al., 2023; Liang *et al.*, 2023; Escamilla-Mejia *et al.*, 2023), Rare earth metals produce a high number of energy levels because they have unfilled 4f shell layers or empty 5d orbitals, while the 4f, 5d, and 6s electrons are close in energy (Lee *et al.*, 2013), exhibits unique properties and functions. Studies have shown (Wang *et al.*, 2011) that the doping modification of rare earth elements can effectively capture photogenerated electrons and inhibit the compounding of photogenerated electrons and holes, which can improve the photocurrent conversion efficiency of photocatalysts in the wavelength range of 300~400 nm, redshift the absorption sidebands, improve the utilization of visible light, and greatly improve the photocatalytic efficiency, and rare earth metal doping has now been widely used in the doping modification of photocatalysis (Zhao and Liu, 2008; Saif *et al.*, 2014; El-Bahy *et al.*, 2009), such as Eu-doped TiO_2 (Juan *et al.*, 2022), La-doped TiO_2(Huang *et al.*, 2017), Nd-doped TiO_2(Wang *et al.*, 2019), Er-doped TiO_2 (Chen *et al.*, 2022).

The preparation of TiO_2 nanomaterials with mesoporous structure is an effective way to enhance photocatalytic activity. Its large specific surface area and well-developed pore structure can facilitate the adsorption of reactants and the absorption of light energy, and it can generate more active reaction centers, thus improving photocatalytic activity (Hou *et al.*, 2020). There are various synthetic methods such as hydrothermal method, template method and sol-gel method to prepare mesoporous TiO_2 nanomaterials, however, it is still challenging to prepare mesoporous TiO_2 nanomaterials with high specific surface area and high crystallinity because the grain growth may lead to collapse of mesoporous structure.

In this study, Re^{3+}(La^{3+}, Sm^{3+}, Nd^{3+}, Gd^{3+})-doped mesoporous titanium dioxide nanopowders were synthesized using a low energy consumption and low pollution hydrothermal method with simple organic reagents and inorganic acids, and their physicochemical properties were characterized by using various characterization tools, and the effects of rare earth ion doping on the crystal structure, surface chemical state, morphology, optical properties and the effects of rare earth ion doping on the crystal structure, surface chemical state, morphology, optical properties and activity of photocatalytic degradation of meta-dimethylhydrazine were investigated in detail. Theintermediates in the degradation process were analyzed by GC-MS, and the reactive radicals were analyzed by radical capture experiments and EPR to deduce the possible mechanism of photocatalysis.

2. Experiment

2.1. Materials and reagents

UDMH, (98%), NDMA(>98%), O_2si, FDMH(>98%), Aladdin Chemicals, Tetrabutyl titanate, Aladdin Chemicals, Inc. (> 99%), HCL (AR), Xi 'an Mipu Chemical Reagent Co., LTD., HNO_3 (AR), Xi 'an Mipu Chemical Reagent Co., LTD., NaOH (AR), Xi 'an Mipu Chemical Reagent Co., LTD., anhydrous ethanol (AR) Tianjin Hengxing Chemical Reagent Co., LTD., La_2O_3, Sm_2O_3, Nd_2O_3, Gd_2O_3, Aladdin Chemical Company 99.99%), isopropyl alcohol, p-benzoquinone, Disodium EDTA, Carbon Tetrachloride, Aladdin Chemicals Co., LTD. (>99.99%), deionized water, laboratory homemade. all reagents are analytical grade reagents, no further treatment is required when used.

2.2. Preparation of photocatalyst

As shown in Figure 1, the rare-earth modified mesoporous TiO_2 nanoparticles were synthesized by a one-step hydrothermal method. 15ml of tetrabutyl titanate was added dropwise to 20 ml of anhydrous ethanol with vigorous stirring for 60 min to obtain a light yellow transparent solution A. A certain concentration of HCL solution was added dropwise to solution A to obtain mixed solution B. A certain amount of lanthanide oxide was weighed and dissolved in HNO_3 to prepare 100ml of 50mM $Re(NO)_3$ solution was set aside, add different volumes of 50mM $Re(NO)_3$ solution drop by drop in solution B, stirred for 30min to ensure that the material ratio of rare earth Re^{3+} to TiO_2 was 0.5%, 1%, 2% and 3% respectively and mixed well, slowly added NaOH solution drop by drop to the above suspension, adjusted the pH to about 7 and stirred for 1h, in turn the suspension was transferred to a 100ml autoclave, put into an oven at 150°C/24h, and the supernatant was decanted after it cooled naturally to room temperature, centrifuged, rinsed with deionized water and anhydrous ethanol, filtered and dried, and ground into powder to obtain the sample TiO_2, 0.5%Re^{3+}-TiO_2, 1%Re^{3+}-TiO_2, 2%Re^{3}+-TiO_2, 3%Re^{3+}-TiO_2 are simply noted as TiO_2, 0.5%Re-TiO_2, 1%Re-TiO_2, 2%Re-TiO_2, 3%Re-TiO_2.

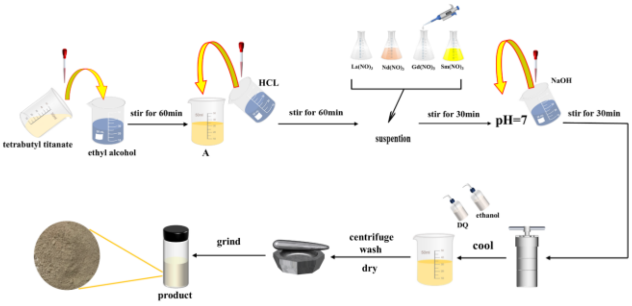

Figure 1. Material preparation process diagram

2.3. Characterization

The physical composition and crystal image of the samples were examined by X-ray diffractometer (XRD, bruker D8 advanced, Germany) with the following operating parameters: Cu target, Kα rays, λ=0.15401 nm, target voltage 40KV, scanning range 5°~90°, scanning speed 5°/min, FT-IR spectroscopy (FT-IR, bruker VERTEX 70, Germany) to measure the FT-IR spectra of the samples in the range of 450 cm^{-1}~4000 cm^{-1}, KBr was used as diluent, and the elemental composition of the material surface was determined by X-ray photoelectron spectrometer (XPS, AXIS ULTRADLD, UK) and analyzed for its chemical valence state, combined with the ability to use the C 1s peak at 284.8 eV for calibration. The surface morphology of the material was observed by a cold emission scanning electron microscope (FESEM, Gemini, Germany) equipped with EDS at a high speed voltage of 15 kV, and the elemental composition and relative content of the material were determined by an energy spectrometer (EDS). The microscopic morphology and crystal structure of the materials were further observed by a high-resolution transmission electron microscope (HRTEM, JEM-2100F, Japan), and the crystalline spacing was analyzed, and the absorption properties of the UV-Vis diffuse reflectance spectra were tested by a UV-Vis spectrometer (UV-Vis DRS, Ocean Optics SB650, USA). PL) steady-state spectra with excitation wavelength of 325 nm, Raman spectra were obtained by nanoraman spectrometer (Naman, HORIBA JY HR-800, France) under 532 nm excitation, the specific surface area of the material was measured by specific surface area and porosity analyzer (JW-BK300, China), and the pore size distribution was calculated by BJH method, and the pore size distribution was calculated by electron paramagnetic resonance spectrometer (EPR, Bruker A300, Germany) to collect electron paramagnetic resonance spectra, detect and analyze free radicals, photoelectrochemical measurements were performed at an electrochemical workstation (Priston P4000, USA) by the chronocurrent method, FDMH, NDMH by high performance liquid chromatography (HPLC, Ultimate 3000, USA)

2.4. Analysis method

The photocatalytic activity of the prepared samples was evaluated by decomposing the dye under a 350W xenon lamp, using a CEL-LAB500E 350W xenon lamp with AM 1.5 filter to simulate sunlight as the catalytic light source, and the light intensity was set to 100 mW/cm^2. The catalyst was stirred for 30 min to ensure the adsorption-desorption equilibrium, and the suspension was centrifuged to measure the absorbance A value of the upper clear layer.

The degradation efficiency R, mineralization efficiency and reaction kinetics of UDMH were used to evaluate the photocatalytic performance of the material with the following equations:

$$R=\left(C_0-C_t\right)/C_0 \quad (1)$$

Where: C0 is the initial concentration of UDMH, mg/L; Ct is the concentration of UDMH in the wastewater at the time of photocatalytic reaction t, mg/L. In addition, the general photocatalyst degradation of organic pollutants is a pseudo primary kinetic reaction with the following equation:

$$\ln\frac{C_0}{C_t}=kt \quad (2)$$

Where: k is the first-order kinetic reaction rate constant, h^{-1} or min^{-1}; t is the time of photocatalytic degradation of UDMH

$$\text{Mineralizationrate}\left(100\%\right)=\frac{\text{TOC}_0-\text{TOC}_t}{\text{TOC}_0} \quad (3)$$

Where: TOC_0 and TOCt represent the concentration of total organic carbon at the initial time and reaction time t. The method used for the determination of UDMH in the experiment was the spectrophotometric method of sodium aminoferricyanide in GB/T 14376-1993 (Zhang *et al.*, 2023), With UV-vis spectrometer (721, Shanghai Instrument Analysis Factory, China), UDMH reacted with sodium aminocyanide to form a red complex with a maximum absorption wavelength of 500 nm, and the concentration of UDMH was determined by the principle that the color depth of the red complex is proportional to the content of UDMH (Zhou *et al.*, 2020). Further assessment of mineralization of methyldimethylhydrazine wastewater by means of a total organic carbon analyzer (vario TOC select, Elementar Analysensysteme GmbH, Germany).

2.5. Photoelectrochemical performance analysis

The photoelectrochemical performance of the photocatalyst was tested by three-electrode system and electrochemical workstation, the photocatalyst was loaded on ITO conductive glass to prepare working electrode, Pt sheet electrode as counter electrode, Ag/AgCl electrode as reference electrode, 0.5 mol/L Na_2SO_4 as electrolyte, and the photoelectrochemical performance was tested by chrono-current method, and the current density was measured under light and dark conditions in turn, and the separation efficiency was judged by The photocurrent changes of photoelectrons and holes in the external circuit after excitation were used to determine the degree of fast response of the material to light and the separation efficiency of photoelectron-hole pairs, the higher the photocurrent, the higher the separation efficiency.

2.6. Free radical capture experiment

According to the basic principle of photocatalysis, the degradation process of organic matter mainly consists of direct oxidation of organic pollutants by photogenerated pairs, or the reaction with surface adsorbed oxygen (O_2) and H_2O/OH^- to generate superoxide radicals(O_2^-) and hydroxyl radical (OH). In order to determine the mechanism of photocatalytic degradation of methyldimethylhydrazine, different radical trapping agents were added to the photocatalytic degradation of methyldimethylhydrazine under the same experimental conditions, and the role of each radical in the photocatalytic degradation process was evaluated by verifying the type of reacting radicals, and this paper mainly used isopropyl alcohol, p-benzoquinone, disodium ethylenediaminetetraacetic acid (Na_2EDTA), and carbon tetrachloride as capture agent of $OH{\cdot}O_2^-h^+$ and e^-, Set the addition concentration at 1 mM and analyze the effect of active species produced by different photocatalysts on the degradation of UDMH wastewater, using the UDMH wastewater degradation system with only the catalyst added as a blank reference, no trapping agent was added and other conditions were kept consistent (Alam *et al.*, 2018).

3. Results and discussions

3.1. *Structural analysis of photocatalysts*

The crystal structure of the samples was studied by X-ray diffractometer (XRD). Figure 2 shows that the XRD spectra of pure TiO_2 and rare-earth Re^{3+}-doped TiO_2 are in basic agreement with the standard card of anatase phase TiO_2 (PDF:21-1272), the characteristic diffraction peaks of each crystal plane family in the spectra are sharp, and the material has good crystallization properties, The 2Ɵ characteristic diffraction peaks at 25.3°, 37.5°, 48.2°, 55.1°, 62.9° correspond to the (101), (004), (200), (105), (204) crystallographic planes of anatase titanium dioxide crystals(Fan *et al.*, 2014), The diffraction peaks of rare earth Re $^{3+}$-doping are not significantly different from those of pure TiO_2, and the diffraction peaks of rare earth oxides do not appear after doping, indicating that the rare earth elements are uniformly dispersed in the TiO_2 phase after doping, and there is no independent phase (Hassan *et al.*, 2012), Considering the radii of Nd^{3+} (0.100 nm), La^{3+} (0.106 nm), Sm^{3+} (0.096 nm), Gd^{3+} (0.094 nm), which are much larger than the radius of Ti4+ (0.068 nm), it is difficult for Re^{3+} to directly enter the lattice of TiO_2 to replace Ti^{4+} to form a stable solid solution, but it is uniformly dispersed in the form of clusters in TiO_2 nanoparticles or in the interstices of the iron-oxygen octahedra of titanium dioxide (Nguyen-Phan *et al.*, 2009). In Figure 2 (b), although the different Re^{3+} doping process did not change the crystalline phase of TiO_2, the diffraction peak half-peak width gradually increased and intensity gradually decreased compared with the undoped sample, and (101) the crystalline surface shifted to a low angle, and in Figure 2 (a), when Nd^{3+} was doped, the doping ratio gradually increased, and the trend of peak broadening and dwarfing became more obvious, the different Re^{3+} doping inhibits the growth of titanium dioxide grains and causes grain refinement, and within a certain doping ratio, the trend of grain refinement is more obvious as the amount of Re^{3+} doping increases. The grain refinement can increase the specific surface area and enhance the oxidation ability of the photocatalyst through the quantum size effect, which will be beneficial to the non-homogeneous photocatalytic reaction.

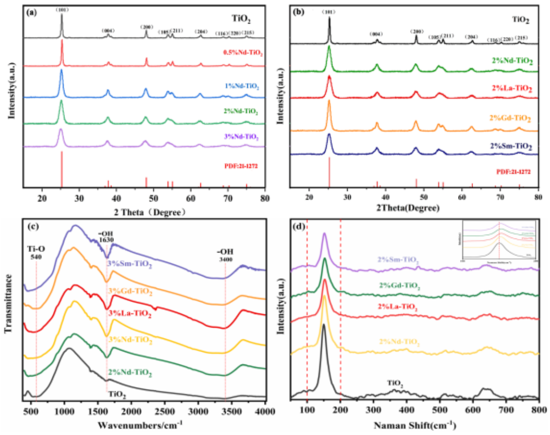

Figure 2. (a) XRD spectra of pure TiO_2 and TiO_2 doped with different concentrations of Nd_{3+} (b) XRD spectra of pureTiO_2 and 2% Re-TiO_2 (Nd^{3+}, La^{3+}, Gd^{3+}, Sm^{3+}) (c) FT-IR spectra of pure TiO_2, 2% Nd-TiO_2 and 3% Re-TiO_2 (Nd^{3+}, La^{3+} , Gd^{3+}, Sm^{3+}) (d) Naman spectra of pure TiO_2 and 2% Re-TiO_2 (Nd^{3+}, La^{3+}, Gd^{3+}, Sm^{3+})

The information of the chemical structure of the samples was further investigated by FT-IR test, and Figure 2 (c) shows that all samples showed three characteristic absorption peaks at 540 cm^{-1}, 1630 cm^{-1}, and 3400 cm^{-1}, which were attributed to the Ti-O stretching vibration in anatase TiO_2, the bending vibration of physisorbed water molecules -OH, and the stretching of surface -OH from water dissociation vibration, compared with pure TiO_2, the characteristic peak at 1630 cm^{-1} is significantly enhanced after doping, and the peak of 3% Nd-TiO_2 is stronger than that of 2% Nd-TiO_2, probably because after Re^{3+} doping, Ti^{4+} replaces Re^{3+} at the rare-earth oxide lattice interface and forms Ti-O-Re bond leading to lattice distortion, which increases the number of surface-OH, and at the same time the Ti-O characteristic peak is red-shifted. The 3440 cm^{-1} characteristic absorption peak indicates that the photogenerated h^+ generated by TiO_2 after photoexcitation reacts with H_2O or OH- to form·OH. The enhancement of the peak at 3440 cm^{-1} after doping indicates that the number of ·OH increases after doping, which is beneficial to the photocatalytic reaction activity, and this change may be due to the increase of specific surface area after Re^{3+} doping. The new characteristic peaks did not appear after doping, and only some of the peaks were broadened and distorted, which is a change in the interaction forces between the groups only after doping, which corroborates with the XRD results.

The crystal structure and surface defects of the samples were further investigated by Naman tests. 144 cm^{-1}(E_g), 197cm^{-1}(E_g), 639cm^{-1}(E_g), 513 cm^{-1}(A_{1g}), and 396 cm^{-1}(B_{1g}) Raman vibrational peaks revealed the synthesis of anatase phase TiO_2 (Kibasomba *et al.*, 2018). After Re^{3+}(Nd^{3+},La^{3+},Gd^{3+},Sm^{3+}) doping,The strongest peak at 144 cm^{-1}(E_g) is obviously weakened, indicating that the particle size of TiO_2 decreases with Re^{3+} doping, and the anatase phase TiO_2 is a tetragonal crystal system, and the change of E_g vibrational peak in the tetragonal crystal system can directly prove the generation of oxygen vacancies (Salari *et al.*, 2011) , The inset in the upper right corner of Figure 2 (d) shows the strongest peak of the E_g pattern for all samples, which is shifted toward the high wave number, indicating that more oxygen vacancies are generated in the doped titanium dioxide nanolattice structure, and the oxygen vacancies can act as electron capture traps to inhibit carrier complexation. In addition, the oxygen vacancies can also form transition energy levels between the conduction band and valence band, reducing the band gap and thus enhancing the visible light response, thus enhancing the photocatalytic activity (Jiang *et al.*, 2012).

3.2. *Morphological analysis of photocatalysts*

From Figure 3, it can be seen that the prepared photocatalysts are porous materials composed of inhomogeneous nanoparticles, and the phenomenon of particle agglomeration occurred in all samples. The prepared pure TiO_2 is a group of irregular block structures with more fragments and cracks, with agglomerated morphology, and the particle size is about 30~40nm. The doping of rare earth Re^{3+} (Nd^{3+}, Sm^{3+}, Gd^{3+}, La^{3+}) has an obvious inhibiting effect on the growth of TiO_2 The grain size of 1%Nd-TiO_2 is about 15~25nm, 2%Nd-TiO_2 is about 10~20nm, 3%Nd-TiO_2 is about 10~15nm, with the increase of Nd^{3+} doping, the trend of grain refinement is more obvious, which is consistent with the xrd results and can be obtained from the increase of specific surface area in Table 1 corroborate (Parveen *et al.*, 2017). In order to determine the actual doping amount of Re^{3+} in Nd-TiO_2, an energy spectrometer (EDS) was used to test and analyze the content of 2% Nd-TiO_2. The peaks identified in the EDS plot corresponded to Ti, O, and Nd elements, and the mass ratio of Nd to TiO_2 was calculated to be 2.03%, which was basically consistent with the expected doping amount, and the EDS results indicated the successful synthesis of 2%Nd-TiO_2 photocatalyst was successfully synthesized.

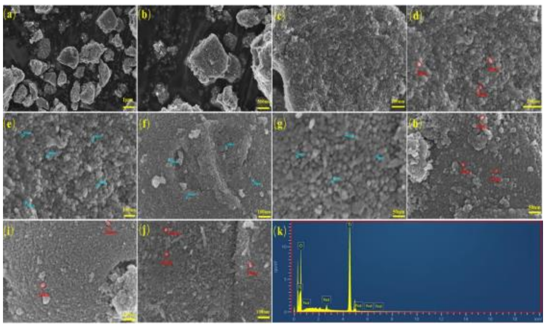

Figure 3. FESEM plots of (a) (b) (c) (d) pure TiO_2, (e) 1%Nd-TiO_2, (f) 2%Nd-TiO_2 , (g) 3%Nd-TiO_2 (h) 3% Sm-TiO_2 , (i) 2%Gd-TiO_2 , (j) 2%La-TiO_2 (k) EDS plots of 2%Nd-TiO_2

HRTEM images can provide finer crystal internal results and analyze the crystalline surface spacing and defects. From Figure 4, The prepared samples have a particle size of about 10~30 nm, and the morphology is an aggregated state of nanoparticles, and the nanoparticles stack up to form porous channels similar to wormholes, which are randomly distributed between the nanoparticles and form a three-dimensional structure, which can increase the specific surface area of the catalyst, and then provide more catalytic reaction active sites, the prepared pure TiO_2 and Re^{3+}-doped TiO_2 lattice stripes are clear, indicating good crystallinity, and the lattice stripe spacing of 0.352 nm, 0.351 nm, and 0.350 nm correspond to the (101) crystallographic plane of anatase TiO_2, and because the radius of Re^{3+} is larger than that of Ti^{4+}, the lattice distortion caused by the doping of Re^{3+}, locally (within the dashed box) lattice stripe produces a slight expansion, and the generated impurity defects or oxygen vacancies can be used as traps for photogenerated electrons or holes to inhibit photogenerated electron-hole complexation and thus enhance photocatalytic activity.

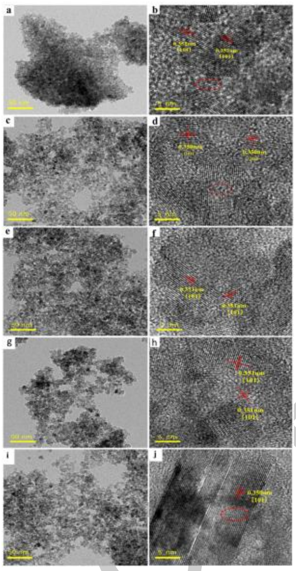

Figure 4. HRTEM images of (a), (b) pure TiO_2, (c), (d) 2%La-TiO_2, (e) , (f) 2%Gd-TiO_2, (g) , (h) 2%Nd-TiO_2, (i) , (j) 2%Sm-TiO_2

The physical and chemical conditions of the catalyst surface directly determine the catalytic reaction active sites and adsorption, which have important effects on the photocatalytic reaction. The specific surface area and pore size distribution of the samples were analyzed by BET method, and the nitrogen adsorption and desorption curves and pore size distribution curves are shown in Figure 5. The specific surface area and pore size (DP) data of the samples are included in Table 1. At lower relative pressures ($P/P_0<0.4$), the adsorption of the material is high, indicating the presence of mesoporous structure, and a type IV curve appears at relative pressures $P/P_0=0.4$~0.8 with H_4 and H_2 hysteresis loops, indicating that the material is a typical mesoporous material (Thommes *et al.*, 2015), containing "ink bottle" interstitial pores. This is consistent with the results of the porous channels in the SEM photographs, where monolayer adsorption occurs mainly on the mesoporous pore walls at low relative pressures, with minimal micropore adsorption; at moderate relative pressures, adsorption increases rapidly and capillary coalescence occurs; and at high relative pressures, adsorption limitation occurs.

Table 1. BET specific surface area (SBET), pore volume and average pore size of the prepared samples

Sample	S_{BET} (m^2/g)	Pore volume (cm^3 /g)	Pore size (nm)	Sample	S_{BET} (m^2/g)	Pore volume (cm^3 /g)	Pore size (nm)
Pure TiO_2	130.5	0.196	5.455	3%Gd-TiO_2	172.4	0.237	4.323
3%Sm-TiO_2	184.8	0.251	3.971	2%Gd-TiO_2	155.4	0.215	4.378
2%Sm-TiO_2	174.3	0.223	4.037	1%Gd -TiO_2	142.2	0.203	4.613
1%Sm-TiO_2	165.2	0.201	4.362	0.5%Gd-TiO_2	133.4	0.196	4.939
0.5%Sm-TiO_2	149.6	0.198	5.016	3%La-TiO_2	163.7	0.218	5.155
3%Nd-TiO_2	187.7	0.230	3.494	2%La-TiO_2	151.1	0.205	5.246
2%Nd-TiO_2	180.3	0.217	3.667	1%La-TiO_2	145.5	0.199	5.363
1%Nd-TiO_2	160.5	0.204	3.697	0.5%La-TiO_2	139.3	0.197	5.433
0.5%Nd-TiO_2	153.8	0.201	3.786				

The pore size distribution diagram shows that the pore size distribution of the prepared samples are all located in the narrow range of 2~10 nm, which indicates that the intermediate pore distribution of the samples is concentrated and uniformly ordered. The specific surface area and pore volume of 3%Sm-TiO_2, 3%Nd-TiO_2 and 2%Nd-TiO_2 are larger, which can expose more active sites in the photocatalytic process and thus enhance the photocatalytic performance.

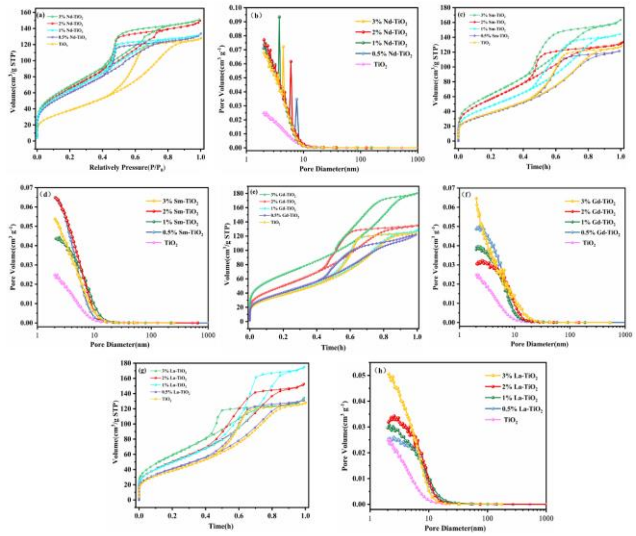

Figure 5. (a) N_2 adsorption-desorption isotherms of pure $TiO_2$2 and Nd-TiO_2, (b) pore size distribution curves of pure TiO_2 and Nd-TiO_2, (c) N_2 adsorption-desorption isotherms of pure TiO_2 and Sm-TiO_2, (d) pore size distribution curves of pure TiO_2 and Sm-TiO_2, (e) N_2 adsorption-desorption isotherms of pure TiO_2 and Gd-TiO_2 , (f) pore size distribution curves of pure TiO_2 and Gd-TiO_2, (g) N_2 adsorption-desorption isotherms of pure TiO_2 and La-TiO2, (h) pore size distribution curves of pure TiO_2 and La-TiO_2.

3.3. *Analysis of chemical composition of photocatalysts*

The elemental nature of the surface layer of the photocatalyst was analyzed by XPS to further determine the presence state of each element, and the total spectra in Figure 6 (a), (b), (c) and (d) show that the materials all contain Ti , Re (Sm, Nd, Gd, La), O and C. Figure 7 (e), (f), (g) and (h) are the XPS spectra of Nd 3d, O 1s, Ti in 2%Nd-TiO_2 2p and C 1s XPS spectra, the characteristic peaks of Nd are located at 983.4 eV and 1003.6 eV, respectively, which represent the bond energies of Nd $3d_{5/2}$ and Nd $3d_{3/2}$ (Yuvakkumar and Hong, 2015), The asymmetric peaks of O 1s appear in two separate peaks at binding energies 530.2eV and 532.4eV, respectively, indicating the existence of two different types of oxygen species on the surface after doping modification, where the strong peak at 530.2eV is the Ti-$O_{lattice}$ chemical bond formed between titanium and oxygen elements in the lattice, corresponding to the lattice oxygen species, and the weak peak at 532.4eV is the Ti-O_{surf} chemical bond formed between titanium and oxygen elements on the surface of the catalyst, corresponding to the lattice oxygen species. elements on the catalyst surface, and the corresponding oxygen species are surface hydroxyl oxygen and oxygen vacancies (Xing *et al.*, 2013). The XPS peaks of Ti 2p at binding energies 458.4 eV and 464.1 eV belong to Ti $2p_{3/2}$ and Ti $2p_{1/2}$, respectively, and the characteristic peaks of Ti $2p_{3/2}$ and Ti $2p_{1/2}$ in the Nd-modified catalysts are shifted towards lower binding energies compared to those of pure TiO_2 at binding energies 458.5 eV and 464.5 eV(Nair *et al.*, 2023), which indicates that the 2% Nd-TiO_2, in addition to a large amount of Ti^{4+}, there is also a small amount of Ti^{3+}, and the radius of Nd^{3+} (0.100 nm) is much larger than Ti^{4+} (0.068 nm) and smaller than O (0.140 nm), so it is difficult for Nd^{3+} to directly enter TiO_2 to replace Ti^{4+}, but Ti^{4+} may replace Nd^{3+} at the rare-earth oxide lattice interface, which can form Ti-O-Nd bond, because Ti^{4+} is more electronegative than Nd^{3+}, it is easy to get electrons and make its characteristic peak move to low binding energy, and part of Ti^{4+} is reduced to Ti^{3+} (Nguyen-Phan *et al.*, 2009). The formation of Ti^{3+} and the oxygen vacancies on the catalyst surface facilitate the photocatalytic activity there is a clear splitting of the C 1s peak, with the strong peak at 284.8 eV being the XPS-calibrated C contamination, while the other two weaker binding energy peaks are formed by the carbon-containing material in the air absorbed by the sample.

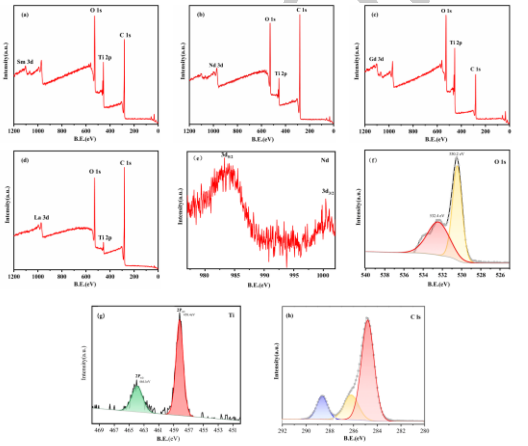

Figure 6. (a) Sm^{3+}-doped TiO_2 photocatalyst XPS full spectrum; (b) Nd^{3+}-doped TiO_2 photocatalyst XPS full spectrum; (c) Gd^{3+}-doped TiO_2 photocatalyst XPS full spectrum;(d) XPS full spectrum of La^{3+}-doped TiO_2 photocatalyst; (e) high-resolution X-ray photoelectron spectra of Nd 3d (f) O 1s (g) Ti 2p (h) C 1s;

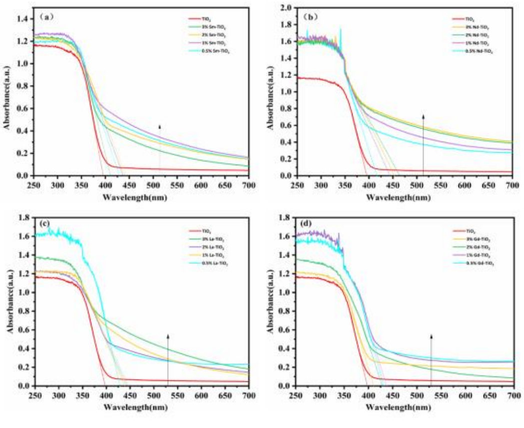

Figure 7. (a) Pure TiO_2 and different concentrations of Sm^{3+}-doped TiO_2 (b) Pure TiO_2 and different concentrations of Nd^{3+}-doped TiO_2 (c) Pure TiO_2 and different concentrations of La^{3+}-doped TiO_2, (d) UV-vis diffuse reflectance spectra of pure TiO_2 and different concentrations of Gd^{3+}-doped TiO_2

3.4. *Optical properties of photocatalysts*

Figure 7 (a), (b), (c), (d) shows the UV-Vis DRS spectra of pure TiO_2 and Sm^{3+}, Nd^{3+}, $La^{3+}$and Gd^{3+} ion doping, the absorption spectra can be used to measure the absorption ability of the photocatalysts to different wavelengths of light, calculate the absorption sideband wavelengths of different photocatalysts, and use the khan formula (Pal and Kryschi, 2016) to find the forbidden band width of the samples, as shown in Table 2.

Table 2. Absorption sidebands and forbidden band widths of pure TiO_2 and different concentrations of Sm^{3+}, Nd^{3+}, Gd^{3+} and La^{3+} doped photocatalysts

Sample	λ/nm	E_g	Sample	λ/nm	Eg
Pure TiO_2	394	3.15	3%Gd-TiO_2	411	3.02
3%Sm-TiO_2	410	3.02	2%Gd-TiO_2	428	2.90
2%Sm-TiO_2	440	2.81	1%Gd -TiO_2	433	2.86
1%Sm-TiO_2	437	2.84	0.5%Gd-TiO_2	431	2.88
0.5%Sm-TiO_2	428	2.89	3%La-TiO_2	446	2.78
3%Nd-TiO_2	456	2.72	2%La-TiO_2	442	2.80
2%Nd-TiO_2	468	2.64	1%La-TiO_2	438	2.84
1%Nd-TiO_2	441	2.82	0.5%La-TiO_2	426	2.91
0.5%Nd-TiO_2	420	2.95			

Compared with pure TiO_2, the doping of Re^{3+} (Sm^{3+}, Nd^{3+}, La^{3+}, Gd^{3+}) redshifts the absorption band edge of the photocatalyst and enhances the absorption effect in both UV and visible regions, and the forbidden band width of pure TiO_2 is 3.15 eV, which is very close to that reported in the literature (Juan *et al.*, 2022), The forbidden band widths are narrowed after doping with Re^{3+}, which can enhance the visible light response of the photocatalyst and thus the photocatalytic activity. The special 4f electron energy level structure of rare earth ions makes the energy values of the ground state and excited state close to each other, and when the 4f electron energy level jumps from the ground state to the excited state, it extends the light absorption wavelength of TiO_2 and enhances the visible light activity of the photocatalyst(Radha *et al.*, 2022), Another reason may be the formation of impurity energy levels between the conduction band and valence band of TiO_2 after the doping of rare earth ions, which changes the relative position of the valence band and conduction band, narrowing the forbidden band width and causing the absorption edge to be red-shifted (Borgarello *et al.*, 1982), The energy difference between the lowest excited state energy level and the ground state energy level in the 4f electron energy levels of different rare earth ions is different, resulting in differences in light absorption ability. 2% Nd-TiO_2 has the most significant light absorption ability in the visible wavelength band greater than 400 nm, and the band gap of the sample is reduced to the greatest extent, with the absorption sideband red-shifted by 74 nm and the corresponding band gap width reduced by 0.51 eV. The above phenomenon may be related to the Nd $4f^4 6s^2$ outer electron arrangement, because its outer electron arrangement does not contain d electrons, $4f^4$ is easy to interact with O 2p orbitals and form impurity energy levels, which can make the photogenerated electrons jump to form photogenerated carriers in multiple steps at lower energy, improve the visible light response and thus enhance the photocatalytic activity.

3.5. *Photogenerated carrier separation analysis*

Stronger photoluminescence peak intensity means higher photogenerated carrier recombination rate and lower separation efficiency of photogenerated electrons from holes in photocatalysts (Kumaravel *et al.*, 2020). It can be seen in Figure 8 that the doping of Re^{3+} did not change the spectral line shape of TiO_2, indicating that the introduction of Re^{3+} did not cause a new luminescence phenomenon, but only affected the intensity of the PL spectrum, and the samples before and after the modification all showed obvious photogenic spectral peaks in the wavelength range of 350~400 nm.

In Figure 8 (a), the relative intensities of the photogenic spectral peaks are in the order of 3%Gd-TiO_2 > TiO_2 > 0.5%Gd-TiO_2 > 2%Gd-TiO_2 > 0.5%Nd-TiO_2 > 1%Gd-TiO_2 > 1%Nd-TiO_2 > 3%Nd-TiO_2 > 2%Nd-TiO_2, This means that the separation efficiency of the photogenerated carriers is 3%Gd-TiO_2 < TiO2 < 0.5%Gd-TiO_2 < 2%Gd-TiO_2 < 0.5%Nd-TiO_2 < 1%Gd-TiO_2 < 1%Nd-TiO_2 < 3%Nd-TiO_2 < 2%Nd-TiO_2, In Figure 8 (b) the relative intensities of the emission spectra are in the order of 3%La-TiO_2 > 2%La-TiO_2 > TiO_2 > 0.5%La-TiO_2 > 0.5%Sm-TiO_2 > 1%La-TiO_2 > 3%Sm-TiO_2 > 1%Sm-TiO_2 > 2%Sm-TiO_2, this means that the separation efficiency of the photogenerated carriers is 3%La-TiO_2 < 2%La-TiO_2 < TiO_2 < 0.5%La-TiO_2 < 0.5%Sm-TiO_2 < 1%La-TiO_2 < 3%Sm-TiO_2 < 1%Sm-TiO_2 < 2%Sm-TiO_2 , The above results show that doping with rare earth Re^{3+} can help to reduce the complex of photogenerated electrons and enhance the photocatalytic activity of TiO_2, which is because the introduction of Re^{3+} can refine TiO_2 nanoparticles and increase the concentration of oxygen vacancies and defects (Nithyaa and Jaya, 2021), However, when the amount of doping exceeds the optimal ratio, the excess Re^{3+} may become the electron complexation center, increasing the electron-hole complexation rate and reducing the photocatalytic activity.

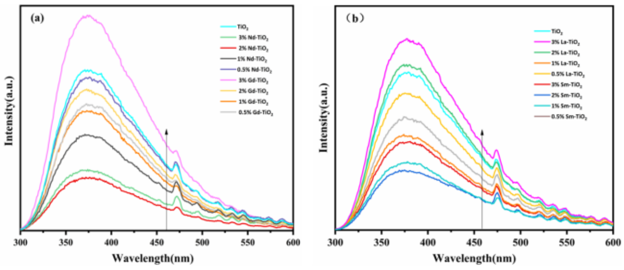

Figure 8. (a) Photoluminescence spectra of pure TiO_2, different concentrations of Nd^{3+}-doped TiO_2 and Gd^{3+}-doped TiO_2 (b) Photoluminescence spectra of pure TiO_2, different concentrations of La^{3+}-doped TiO_2 and Sm^{3+}-doped TiO_2

Generally speaking, the stronger the photocurrent response, the more efficient the separation of photogenerated electrons from holes, which also means the stronger the photocatalytic activity (Zhu *et al.*, 2020). According to the method of 2.5, pure TiO_2 and 1%Gd-TiO_2, 1%La-TiO_2, 2%Nd-TiO_2, 2%Sm-TiO_2 photocatalysts were selected to prepare working electrodes, and the I-t curves were tested under the conditions of 20 s each of light and dark, as shown in Figure 9, all the five materials had a fast light response, and constant photocurrent values could be obtained without delay in the light phase, and in the the current drops rapidly in the light-avoidance phase and maintains a stable value, indicating that the prepared electrode materials are sensitive to light response. From the Figure, it can be seen that the photocurrent response of pure TiO_2 is the weakest, from high to low, 2%Nd-TiO_2, 2%Sm-TiO_2, 1%La-TiO_2 and 1%Gd-TiO_2. This result is consistent with the results of PL spectrum test and degradation test, which indicates that the degradation performance of the photocatalyst is closely related to the carrier separation efficiency.

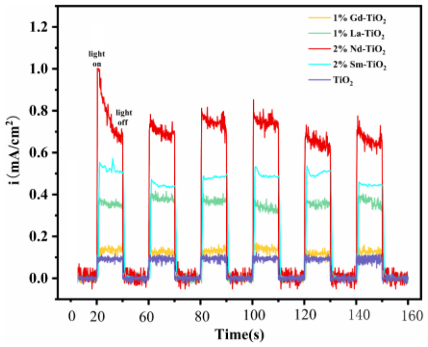

Figure 9. Photocurrent density plots of pure TiO_2, Gd-TiO_2, La-TiO_2, Nd-TiO_2, Sm-TiO_2

3.6. *Photocatalytic activity*

3.6.1. UDMH degradation effect of rare earth modified titanium dioxide

A 350W xenon lamp was used as a simulated light source to degrade UDMH wastewater under simulated sunlight to evaluate the catalytic degradation performance of the samples. The photocatalytic degradation of UDMH wastewater experiment was set up according to 2.4 by adding 3 g of catalyst to the reaction vessel and 50 ml of 100 mg/L UDMH wastewater. As shown in Figure 10 and Table 3, the natural degradation of 100 mg/L UDMH wastewater under simulated sunlight was almost negligible if no photocatalyst was added, and the degradation rate of the prepared pure TiO_2 to UDMH was 51.1%, and the photocatalytic activities of the samples doped with rare earths were all improved compared with pure TiO_2, and the photocatalytic activities were closely related to the amount of rare earth doping. 3%Nd-TiO_2, 2%Nd-TiO_2, 1%Nd-TiO_2, and 0.5%Nd-TiO_2 had 84.5%, 93.3%, 82.1%, and 70.3% degradation rates, respectively, and the doping amount was below 2%, with the increase of Nd^{3+} content, the number of traps in the catalyst that could capture photogenerated carriers increased, and the photogenerated electrons and holes could be separated effectively to make the photocatalytic activity enhanced, and the photocatalytic The catalytic activity is enhanced, and when the n(Nd):n(TiO_2) is greater than 2%, the excess Nd^{3+} will form a large number of Ti-O-RE bonds, which will reduce the concentration of surface oxygen vacancies and defects, and will become the complex center of photogenerated carriers(Liang *et al.*, 2020), The photocatalytic activity is reduced, and from the kinetic analysis of the photocatalytic process, the degradation reaction of UDMH follows a pseudo-kinetic first-order model, and the kinetic constants k values corresponding to the optimal doping amounts of pure TiO_2 and Nd, Sm, La, and Gd under simulated visible light conditions are related as follows: 2%Nd-TiO_2(k=0.25074min^{-1}) > 2%Sm-TiO_2(k=0.18512min^{-1}) > 1%La-TiO_2(k=0.14837min^{-1}) > 1%Gd-TiO_2(k=0.13913min^{-1}) > TiO_2(k=0.06332min^{-1}), It is obvious that 2%Nd-TiO_2 has the highest kinetic constant, which is consistent with the previous conclusion of photocatalytic activity. Since 2%Nd-TiO_2 exhibited the highest photocatalytic efficiency, all the following experiments were conducted to further investigate the photocatalytic performance. As shown in Figure 11, to further evaluate the mineralization effect of 2%Nd-TiO_2 on UDMH, it was verified by TOC, and the TOC degradation rate of UDMH wastewater could reach 84.8% under simulated sunlight irradiation.

Table 3. Degradation rates (DR%), reaction rate constants (K), and linear regression coefficients (R2) of pure TiO_2, Gd-TiO_2, La-TiO_2, Nd-TiO_2, and Sm-TiO_2 for the degradation of UDMH

Samples	DR%	K(h^{-1})	R^2
Pure TiO_2	51.1	0.06332	0.99104
3%Sm-TiO_2	80.4	0.13755	0.98164
2%Sm-TiO_2	90.3	0.18512	0.96206
1%Sm-TiO_2	70.9	0.10395	0.99324
0.5%Sm-TiO_2	61.7	0.08493	0.99061
3%Nd-TiO_2	84.5	0.20067	0.97392
2%Nd-TiO_2	93.3	0.25074	0.97841
1%Nd -TiO_2	82.1	0.17508	0.98384
0.5%Nd -TiO_2	70.3	0.11279	0.96998
3%Gd-TiO_2	55.4	0.07484	0.98417
2%Gd-TiO_2	70.3	0.10463	0.98417
1%Gd-TiO_2	79.6	0.13913	0.97937
0.5%Gd-TiO_2	65.4	0.08498	0.98291
3%La-TiO_2	52.3	0.07019	0.99587
2% La-TiO_2	62.3	0.07348	0.99242
1% La-TiO_2	81.1	0.14837	0.97897
0.5% La-TiO_2	60.6	0.08381	0.99227

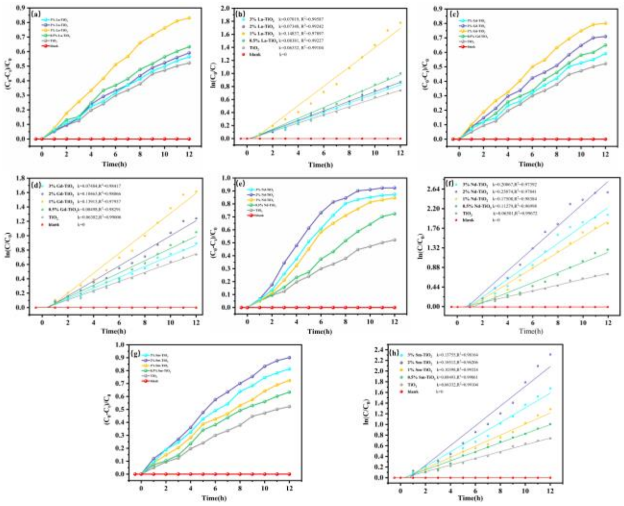

Figure 10. Photocatalytic degradation effect and kinetic linear fit of pure TiO_2, Gd-TiO_2, La-TiO_2, Nd-TiO_2, Sm-TiO_2

3.6.2. Degradation effect of FDMH and NDMA

The concentrations of NDMA and FDMH were tested according to the HPLC method previously studied by the group (Zhou *et al.*, 2021), The initial samples contained a small amount of NDMA and FDMH, and the trends of NDMA and FDMH were basically the same, first rapidly increasing and then slowly decreasing, and the rate of

FDMH and NDMA generation by UDMH was greater than the rate of photocatalytic degradation of both at the initial stage, and both NDMA and FDMH reached the maximum concentration around 3h. At this time, the generation rate and degradation rate were almost equal, and the reaction gradually reached After that, the rate of photocatalytic degradation was greater than the rate of generation, and the concentration gradually decreased slowly, and the yield of FDMH was significantly higher than that of NDMA, which might be because FDMH is an intermediate product of UDMH into NDMA, and it is easier to form NDMA from FDMH than from UDMH(Huang *et al.*, 2019), NDMA and FDMH were completely degraded at around 9h and 10h, respectively, indicating that UDMH could be completely mineralized.

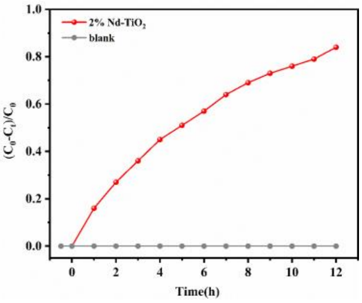

Figure 11. TOC detection during the degradation of UDMH wastewater

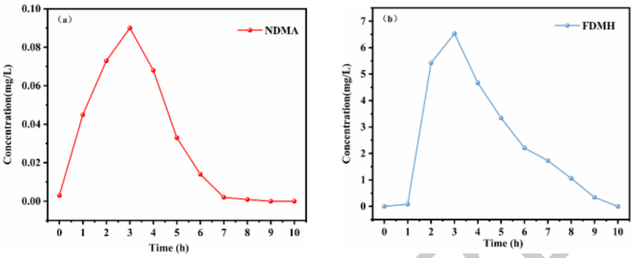

Figure 12. Degradation effect of 2%Nd-TiO2 on NDMA and FDMH

3.6.3. *Stability of photocatalysts*

In addition to the photocatalytic activity, the stability of the photocatalyst is also an important evaluation criterion in the process of practical application. 50 ml of UDMH wastewater with a concentration of 50 mg/L was configured, and the recovery cycle experiment was conducted with 2%Nd-TiO_2 under the irradiation of 350 W xenon lamp, and the supernatant was decanted at the end of each cycle, centrifuged and rinsed with deionized water and anhydrous ethanol, dried at 70°C and then recirculated, as shown in Figure 12 (a) shows, the degradation efficiency of four cycles for UDMH was 94.55%, 89.36%, 87.86% and 85.7% in order to further confirm the stability of 2%Nd-TiO_2, the 2%Nd-TiO_2 after UDMH cycle test was characterized by XRD and FTIR spectra, the results of XRD showed that the crystal structure of 2%Nd-TiO_2 did not significantly changed, and the FTIR results showed that the functional groups of 2%Nd-TiO_2 did not change significantly, and the photocatalytic activity of 2%Nd-TiO_2 was observed to decrease by 8.85% after four cycles, probably due to partial mass loss during centrifugation, washing and drying, rather than due to its passivation, and 2%Nd-TiO_2 has good stability as an efficient visible photocatalyst, but it also indicates that the powdered catalyst has the defects of tedious operation and easy loss in recoverability.

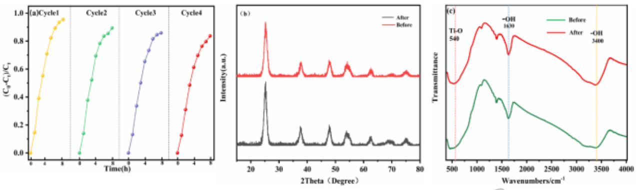

Figure 13. (a) Recycling test results of 2%Nd-TiO2, (b) XRD patterns before and after 2%Nd-TiO2 test, (c) FTIR patterns before and after 2%Nd-TiO2 test

3.7. *Active substance identification*

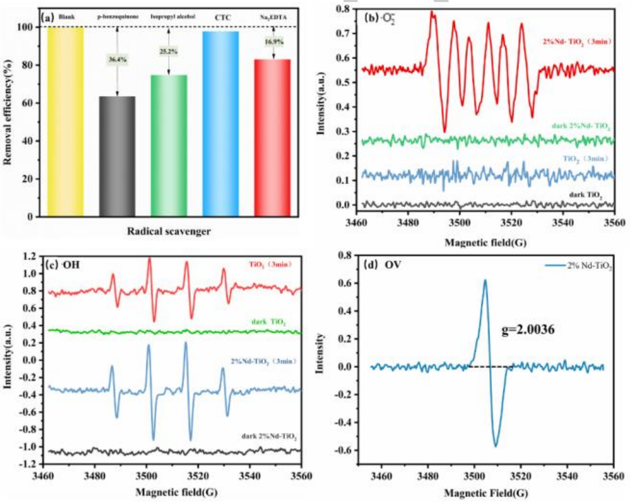

Figure 14. (a) active substance capture experiments based on visible light conditions to degrade UDMH, (b) EPR spectra of $\cdot O_2$- adducts captured under dark and visible light irradiation for 3 min , (c) EPR spectra of OH adducts captured under dark and visible light irradiation for 3 min, (d) EPR spectra of oxygen vacancies of 2%Nd-TiO_2

The experimental conditions were designed as described in 2.6, 2%Nd-TiO_2 was selected as the photocatalyst, and the degradation rate of UDMH decreased in all groups after adding the trapping agent, indicating that, OH,$\cdot O_2^-$, photogenerated h+ and photogenerated e- participated in the photocatalytic degradation process , The values of the effect of isopropyl alcohol, p-benzoquinone, Na2EDTA, and carbon tetrachloride on the degradation efficiency of UDMH were 36.4 %, 25.2 %, 16.9 %, and 1.23 %, in that order. Therefore, the photocatalytic effect of active species on UDMH diminishes in the order of O_2^->·OH> h^+> e^-.The effect of photogenerated e^- on UDMH is small and can be ignored, $\cdot O_2^-$and·OH being the main active species. The EPR technique was used to identify and detect the $\cdot O_2^-$and ·OH radicals, and 100 mM DMPO was used as the trapping agent, as shown in Figure 13 (a) and (b) under dark conditions, there was no obvious $\cdot O_2^-$and ·OH radical signal in the EPR, and after 3 min of light, a four-peak EPR signal of 1:2:2:1 for DMPO-·OH was observed for both TiO2 and 2%Nd-TiO_2, and the DMPO-·O_2^-six-peak signal, indicating that $\cdot O_2^-$ and ·OH radicals play a major role in this photocatalytic process, which is consistent with the results of the trapping experiments. 2%Nd-TiO_2 exhibits a stronger·O_2^- and ·OH signal compared to TiO_2, indicating that the concentration of both·$O_2^-$and·OH increases under visible light excitation after doping, g=2.0036 EPR signal of 2%Nd-TiO_2 in 13(d) indicates the presence of oxygen vacancies in the lattice (Santara *et al.*, 2014), both the increase in the concentration of active species and the generation of oxygen vacancies are beneficial to enhance the photocatalytic activity.

3.8. *Analysis of photocatalytic degradation mechanism*

From the analysis of photocatalyst morphological structure, spectral absorption performance and photogenerated carrier separation, it has been confirmed that Re^{3+} doping improves the visible light response of TiO_2 and increases the photogenerated electron yield, the energy band edge position of photocatalyst can be calculated by the formula ECB=E_{VB}-E_g, the energy band structure of TiO_2 and 2% Nd-TiO_2 is shown in Figure 14, combined with the spectral absorption performance and E_{VB}=2.91eV for pure TiO_2 measured by XPS spectroscopy, Eg=3.15eV from UV-Vis DRS, and E_{CB}=-0.24eV calculated. EVB = 2.41eV for 2% Nd-TiO_2, UV-Vis DRS gives Eg = 2.64 eV, and E_{CB} = -0.23eV is calculated, the E_{CB} before and after doping are more negative than the oxidation potential of O_2 /·O_2^- (-0.046 eV vs. NHE), and the photo-generated electrons (e^-) can react with O_2 to form , and the E_{VB} before and after doping are larger than the reduction potential of H_2O/·OH (2.4 eV vs. NHE), so h^+ can oxidize H_2O and OH- directly to OH (Yang *et al.*, 2022).

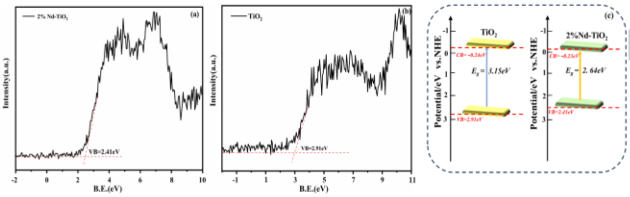

Figure 15. (a) VB-XPS spectrum of 2%Nd-TiO2 (b) VB-XPS spectrum of TiO2 *(*c) Schematic diagram of the energy band structure of 2%Nd-TiO_2 and TiO_2

Figure 15 shows the mechanism diagram of rare earth single doped TiO_2 photocatalytic degradation of UDMH, in pure TiO_2, under the excitation of UV light, the photocatalyst undergoes electron leap from O 2p to Ti 3d orbitals, Re^{3+} doping forms impurity energy level at the bottom of TiO_2 conduction band, which reduces the band gap width and extends the light absorption range to visible light region, under visible light irradiation, photogenerated electrons undergo O 2p to Nd 4f orbital electron leap, the electrons detached from the valence band are more likely to reach the conduction band, producing photogenerated electron-hole pairs, the unfilled 4f orbitals of Re^{3+} can capture photogenerated electrons, hindering the compounding of photogenerated electrons and holes, the resulting excited state of Re^{3+} can be oxidized with the photogenerated electrons produced in the valence band of TiO_2, Re^{3+} captured photogenerated electrons are reduced to Re^{2+}, and The reduction reaction with the hole in the conduction band generates Re^{4+} (Liang *et al.*, 2020), Reaction of photogenerated electrons with O_2 adsorbed on the surface of the receptor, forming $(O_2)^-_{adsorb}$. OH and·OOH are formed by reacting with H_2O and H^+, while the cavity h^+ reacts with OH^- or H_2O adsorbed on the surface to form ·OH, and it has been shown that .OOH, which may be generated during the photocatalytic process, can participate in the UDMH reaction (Wang *et al.*, 1999; Liao and Gurol 1995), The generated·$(O_2)_{adsorb}$·OH.OOH etc. are strongly oxidizing and can convert UDMH into CO_2, H_2O and other small molecule products. The photocatalytic degradation of UDMH wastewater may involve the following processes:

$$\mathrm{Re-TiO_2 \rightarrow e^- + h^+}$$
$$\mathrm{Re^{3+} + e^- \rightarrow Re^{2+}}$$
$$\mathrm{Re^{3+} + h^+ \rightarrow Re^{4+}}$$
$$\mathrm{h^+ + H_2O \rightarrow OH + H^+}$$
$$\mathrm{h^+ + OH^- \rightarrow OH}$$
$$\mathrm{e^- + (O_2)_{adsorb} \rightarrow (O_2)^-_{adsorb}}$$
$$\mathrm{(O_2)^-_{adsorb} + H_2O \rightarrow OOH + OH^-}$$
$$\mathrm{(O_2)^-_{adsorb} + 2H^+ \rightarrow OH + OH^-}$$
$$\mathrm{(O_2)^-_{adsorb}\ /OH / OOH + UDMH}$$
$$\mathrm{\rightarrow Intermediate\ products \rightarrow CO_2 + H_2O + OMPO}$$

It has also been reported(Li *et al.*, 2014) that TiO_2 is able to produce Ti3+ under the effect of photoexcitation and is able to convert the lattice oxygen Olattice inside the crystal to surface adsorbed oxygen (O_2) adsorbe after the transition state of O (O_2) $_{inter}$, which in turn can produce oxygen vacancies Ov with $(O_2)^{2-}_{adsor}$, the generated Ti^{3+} will produce a positive charge center, and to achieve charge balance, this center will adsorb photogenerated electrons, reducing the compounding efficiency of photogenerated carriers, can adsorb OH^-, and OH^- reacts with h^+ to produce more ·OH to participate in the UDMH degradation reaction (El-Bahy *et al.*, 2009), and the generated oxygen vacancies can act as trapping sites for photoexcited electrons and promote the separation of electrons and holes (Ni *et al.*, 2021), It can form an intermediate energy band between the conduction band and valence band of TiO_2 to reduce the band gap and enhance the response of visible light (Zhang *et al.*, 2011), thus improving the photocatalytic activity, and the formation of Ti^{3+} and oxygen vacancies on the catalyst surface are favorable to the photocatalytic activity.

$$(O_2)_{inter}\ f\ \ (O_2)_{inter}\ f\ \ (O_2)^{2-}_{adsor} + O_v$$

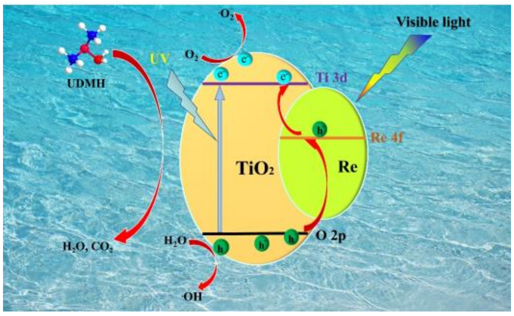

Figure 16. Schematic diagram of the possible mechanism of degradation of UDMH by Re-TiO_2 under visible light

3.9. *Analysis of UDMH degradation pathways*

The degradation products were studied by GC-MS after 120 min of visible light irradiation, and the details of the identified products have been listed in Table 4. The possible degradation pathways of UDMH are shown in Figure 17. In brief, the degradation pathways of UDMH mainly include bond breaking, condensation, oxidation, and hydrolysis, and UDMH in Figure 16 proceeds along the following transformation pathways from top to bottom: In the first pathway, UDMH is directly converted to $(CH_3)_2NNH{\cdot}OOH$ by the action of free radicals, and then H_2O is directly removed to generate NDMA, which is further oxidized to dimethylamine and HCHO. In the second pathway, $^{\cdot}$OH attacks the N-N bond of UDMH and breaks it to form the dimethylamino radical $(CH_3)_2N{\cdot}$and the amino radical NH_2, and $NH_2{\cdot}$ couples with $CH_3{\cdot}$ to form methylamine which is then oxidized to formamide, which is further hydrolyzed to form NH_3 and HCOOH, and the dimethylamino radical $(CH_3)_2N{\cdot}$ reacts with the formyl $HCO{\cdot}$ to form dimethylformamide, and further react to form methylamine, HCHO and $NO_2{\cdot}$ In the third path, ·OH attacks the C-N bond of UDMH and breaks it to form $CH_3{\cdot}$ and methylhydrazine radical, which is oxidized to form methanol and further oxidized to form CH_2OH, which is coupled with $CH_3{\cdot}$ to form ethanol, and methylhydrazine radical $\cdot CH_2NHNH_2$ is oxidized to formylhydrazine radical $(H_2CO{\cdot})(CH_3)NNH_2$, which is coupled with $CH_3{\cdot}$ to produce methylformylhydrazide, which reacts with formamide to form the cyclic compound 1-methyl-1H-1,2,4-triazole. In the fourth pathway, OH attacks the N-H bond of UDMH, which is converted to $(CH_3)_2NN{\cdot}H$ and further oxidized to form $(CH_3)_2N^+{=}N^-$, which is dehydrated to form NDMA after reacting with the reactive group $^{\cdot}$OOH, which is further oxidized to dimethylamine and HCHO. In the fifth path, UDMH and HCHO undergo condensation reaction to produce FDMH and H_2O directly, FDMH is oxidized to produce NDMA, NDMA is further oxidized to dimethylamine, HCHO, and in another case, FDMH is oxidized to produce acetaldehyde dimethylhydrazone, acetaldehyde dimethylhydrazone is further oxidized to produce methylamine, HCHO, NO_2. As the photocatalytic reaction continues, the intermediate is further mineralized to produce NH_4^+,NO_3^-,CO_2 and H_2O.

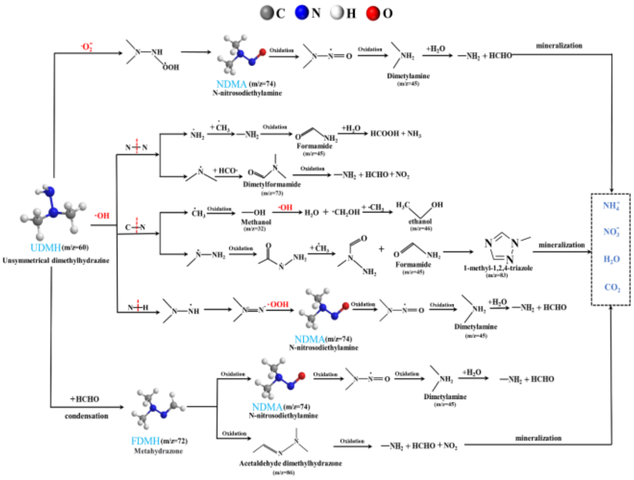

Figure 17. Possible pathways of degradation of UDMH under visible light

Table 4. The intermediate products for the degradation of UDMH

Products*	Molecular formula	Measured mass (m/z)	CAS	Chemical structure
methylenehydrazine	C3H8N2	72	2035-89-4	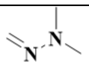
Methanol	CH4O	32	67-56-1	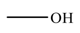
Dimethylamine	CH7N	45	124-40-3	
Ethanol	C2H6O	46	64-17-5	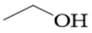
Acetaldehyde dimethylhydrazone	C4H10N2	86	7422-90-4	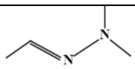
Formamide	CH3NO	45	75-12-7	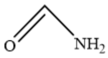
1-methyl-1,2,4-triazole	C3H5N3	83	6086-21-1	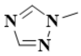
N-nitrosodiethylamine	C2H6N2O	74	62-75-9	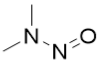
Dimethylformamide	C3H7NO	73	68-12-2	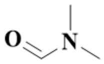

**Ranked by peak intensity.*

4. Conclusion

In summary, a series of mesoporous pure TiO_2 and $Re^{3+}(Sm^{3+}, Nd^{3+}, La^{3+}, Gd^{3+})$-doped TiO_2 nanoparticles were prepared by a simple hydrothermal method, and the photocatalytic activity of these samples was investigated by degradation of UDMH, and the results showed that rare earth ion doping had a great influence on the photocatalytic activity, and 2%Nd-TiO_2 showed the highest photocatalytic efficiency the good photocatalytic degradation effect can be attributed to its smaller grain size, larger specific surface area, enhanced visible light response after doping, and increased number of oxygen vacancies with minimal carrier complex probability, which made it show good degradation performance on UDMH through synergistic effect, and 2%Nd-TiO_2 did not show significant degradation performance after four The 2%Nd-TiO_2 did not show any significant activity loss after four cycles, indicating that it possesses excellent recyclable performance. In addition, according to radical capture experiments and EPR, the main active species in photocatalytic reactions are $\cdot O_2^-$ and $\cdot$OH, The intermediates of UDMH were analyzed and the degradation pathways of UDMH were proposed. The photocatalytic degradation of UDMH by Re^{3+}(Sm^{3+}, Nd^{3+}, La^{3+}, Gd^{3+})-doped mesoporous TiO_2 is a well-established method.

References

Alam U., Khan A., Al D., Bahnermann D. and Muneer M. (2018). *RSC Advances*, **8**(31), 17582–17594.

Borgarello E., Kiwi J., Gratzel M., Pelizzetti E. and Visca M. (1982). *Journal of the American Chemical Society*, **104**(11), 2996–3002.

Byrne C., Subramanian G. and Pillai S.C. (2018). *Journal of Environmental Chemical Engineering*, **6**(3), 3531–3555.

Carlsen L., Kenessov B.N., Batyrbekova S.Y., Kolumbaeva S.Z. and Shalakhmetova T.M. (2009). *Environmental Toxicology and Pharmacology,* **28**(3), 448–452.

Chen J., Chen L., Wang X., Sun J., Chen A.Y. and Xie X.F. (2022). *Applications of Surface Science*, **596**, 153655.

El-Bahy Z.M., Ismail A.A., Mohamed R.M.J. (2009). *Hazardous Materials,* **166**(1), 138–143.

Escamilla-Mejia J.C., Hidalgo-Carrillo J., Martin-Gomez J., Lopez-Tenllado F.J., Estevez-Toledano R.C., Marinas. A. and Urbano F.J. (2023). *Catalysis Today*, **413**.

Fan W.Q., Bai H.Y., Zhang G.H., Yan Y.S., Liu C.B. and Shi W.D. (2014). *Crystengcomm*, **16**(1), 116–122.

FleMing E.C., PenningtFlemon J.C., Wachob B.G., Howe R.A. and Hill D.O. (1996). *Journal of Hazardous Materials,* **51**(1-3), 151–164.

Gopinath K.P., Madhav N.V., Krishnan A., Malolan R. and Rangarajan G.J. (2020). *Environmental Management*, **270**, 110906.

Hassan M.S., Amna T., Yang O.B., Kim H.C. and Khil M.S. (2012). *Ceramic Interfaces*, **38**(7), 5925–5930.

Hou H.L., Shao G., Yang W.Y. and Wong W.Y. (2020). *Progress in Materials Science*, **113**.

Huang D., Liu X.X., Wang X.J., Zuo C.S., Xie Z. and Gao X. (2019). *Chemical Physics*, **522**, 220–227.

Huang Y., Cao J.J., Kang F., You S.J., Chang C.W. and Wang Y.F. (2017). *Aerosol and Air Quality Research*, **17**(10), 2555–2565.

Ismagilov Z.R., Kerzhentsev M.A., Ismagilov I.Z., Sazonov V.A., Parmon V.N., Elizarova G.L., Pestunova O.P., Shandakov V.A., Zuev Y.L., Eryomin V.N., Pestereva N.V, Garin F. and Veringa. H.J. (2002). *Catalysis Today*, **75**(1-4), 277–285.

Jiang X.D., Zhang Y.P., Jiang J., Rong Y.S., Wang Y.C., Wu Y.C., and Pan C.X. (2012). *Journal of Materials Chemistry C*, **116**(42), 22619–22624.

Juan J.L.X., Maldonado C.S., Sanchez R.A.L. Diaz O.J.Z. Ronquillo M.R.R., Sandoval-Rangel L., Aguilar N. P., Delgado N.A.R and Martinez-Vargas D.X. (2022). *Catalysis Today*, **394**, 304–313.

Kibasomba P.M., Dhlamini S., Maaza M., Maaza M., Liu C.P., Rashad M.M., Rayan.D.A. and Mwakikunga B.W. (2018). *Results in Physics*, **9**, 628–635.

Kumaravel V., Rhatigan S., Mathew S., Michel M.C., Bartlett J., Nolan M., Hinder S.J., Gasco A., Ruiz-Palomar C. and Hermosilla D. (2020). *Journal of Physics: Materials*, **3**(2), 025008.

Lee D.Y., Kim J.T., Park J.H., Kim Y.H., Lee I.K., Lee M. H., Kim B.Y. (2013). *Current Applied Physics*, **13**(7), 1301–1305.

Li Y.F., Aschauer U., Chen J. and Selloni A. (2014). *Accounts of Chemical Research*, **47**(11), 3361–3368.

Liang J.C., Wang J.Y., Song K.X., Wang X.F., Yu K.F. and Liang.C. (2020). *Journal of Rare Earths*, **38**(2), 148–156.

Liang J.C., Wang J.Y., Yu K.F., Song K.X., Wang X.F., Liu W.P., Hau J.Z. and Liang C. (2020). *Chemical Physics*, **528**.

Liang R.H., Hu Z.Z., Wu H.Z., Li S.S., Zhang X.Y., Arotiba O.A. and Zhou M.H. (2023). *Separation and Purification Technology*, **314**.

Liao C.H. and Gurol M.D. (1995). *Environmental Science & Technology*, **29**(12), 3007–3014.

Liu Z.J., Hu X.P., He Z. and Wu J.J. (2012) *Energies*, **5**(8), 3126–3136.

Malik P., Sharma D. and Jajpura L. *Advanced Materials and Processes Technology*

Nair P.R., Ramirez C.R.S., Pinilla M.A.G., Krishnan B., Avellaneda D.A., Pelaes R.F.C. and Shaji S. (2023). *Applied Surface Science*, **623**.

Nguyen-Phan T.D, Song M.B., Kim E.J. and Shin E.W. (2009). *Microporous and Mesoporous Materials*, **119**(1-3), 290–298.

Ni J.X., Wang W., Liu D.M., Zhu Q., Jia J.L., Tian J.Y., Li.Z.Y., Wang X. and Xing Z.P.(2021). *Journal of Hazardous Materials*, **408**.

Nithyaa N. and Jaya N.V. (2021). *Applied Physics A: Materials Science & Processing*, **127**(1).

Pal N.K. and Kryschi C. (2016). *Chemosphere*, **144**, 1655–1664.

Paradisi E., Gualtieri M.L., Veronesi P., Dami V., Lorenzi G., Cioni A., Baldi G. and Leonelli C. (2023). *Advanced Materials and Processes Technology*, **6**(7), 5448–5459.

Parveen B., Hassan M., Atiq S., Riaz S., Naseem S. and Toseef M.A. (2017). *Progress in Natural Science*, **27**(3), 303–310.

Radha E., Komaraiah D., Sayanna R. and Sivakumar J. (2022). *Journal of Luminescence*, **244**.

Rahman K.H., Kar A.K., Chen K.C. and Chen C.J. (2023). *Nanotechnology*, **34**(24).

Rashid J., Bhatti T.T., Hassan M., Barakat M.A., Kumar R. and Xu M. (2023). *Fuel*, **346**.

Rueda-Marquez J.J., Levchuk I., Ibanez P.F. and Sillanpaa M.J. (2020). *Cleaner Production Letters,* **258**.

Saif M., Aboul-Fotouh S.M.K., El-Molla S.A., Ibrahim M.M. and Ismail L.F.M. (2014). *Spectrochimica Acta Part A: Molecular and Biomolecular Spectroscopy*, **128**, 153–162.

Salari M., Konstantinov K. and Liu H.K. (2011). *Journal of Materials Chemistry*, **21**(13), 5128–5133.

Santara B., Giri P., Dhara S., Imakita K. and Fujii M. (2014). *Journal of Physics D: Applied Physics*, **47**(23).

Sgroi M., Vagliasindi F.G.A., Snyder S.A. and Roccaro P. (2018). *Chemosphere,* **191,** 685–703.

Thommes M., Kaneko K., Neimark A.V., Olivier J.P., Rodriguez-Reinoso F., Rouquerol J. and Sing K.S.W. (2015). *Pure and Applied Chemistry*, **87**(9-10), 1051–1069.

Wang B.S., Hou H. and Gu Y.S. (1999). *Chemical Physics Letters*, **309**(3-4), 274–278.

Wang S., Wang Z.Y., Wang Y., Xia C.H., Hong E., Bai L.M., Li T. and Wang B.Q. (2019). *Science of the Total Environment*, **652**, 85–92.

Wang Y.J., Shi R., Lin J. and Zhu Y.F. (2011). *Energy & Environmental Science*, **4**(8), 2922–2929.

Xing M., Fang W., Nasir M., Ma Y.F., Zhang J.L. and Anpo M. (2013). *Journal of Catalysis*, **297**, 236–243.

Yang W.X., Ma G.Z., Fu Y., Peng K., Yang H.L., Zhan.X.Q., Yang W.Y., Wang L. and Hou H.L. (2022). *Chemical Engineering Journal*, **429**.

Yuvakkumar R. and Hong S.J.I. (2015). *Journal of Sol-Gel Science and Technology*, **73**, 511–517.

Zhang X., Guo Z.R., Sun P.F., Liu X.Y., Luo Z., Li J.Y., Zhang D.X. and Xu X.Y. (2023). *Separation and Purification Technology*, **312**.

Zhang Z.K., Bai M.L., Guo D.Z., Hou S.M. and Zhang G.M. (2011). *Chemical Communications*, **47**(29), 8439–8441.

Zhao Z.Y., Liu Q.J. (2008). *Journal of Physics D: Applied Physics*, **41**(8).

Zhou F. and Ren X. (2020). *Journal of Environmental Science and Health, Part A: Toxic/Hazardous Substances & Environmental Engineering*, **55**(3), 239–255.

Zhou F., Ren X.H., Qiang H.F., Zeng Y.Z. and Fan M.M. (2021). *Cailiao Gongcheng*, **49**(11), 171–178.

Zhu Z., Ma C.C., Yu K.S., Lu Z.Y., Liu Z., Huo P.W., Tang X. and Yan Y.S. (2020). *Applied Catalysis, B: Environmental*, **268**.